

Article

The Quick Removal of Toxic Dye Molecules by an Efficient Adsorptive BiOI/Bi₂MoO₆ Heterostructure

Tasie Ebenezer Onyedika^{1,2,†} , Mengying Xu^{1,2,3,4,†}, Yichao Deng², Yang Liu², Lian Li^{2,5}, Pier-Luc Tremblay^{1,2,5,*}  and Tian Zhang^{1,2,3,5,6,*} ¹ Shaoxing Institute for Advanced Research, Wuhan University of Technology, Shaoxing 312300, China² School of Chemistry, Chemical Engineering, and Life Science, Wuhan University of Technology, Wuhan 430070, China³ School of Resources and Environmental Engineering, Wuhan University of Technology, Wuhan 430070, China⁴ Zhejiang Xingguang Pharmaceutical Co., Ltd., Shaoxing 312400, China⁵ Sanya Science and Education Innovation Park, Wuhan University of Technology, Sanya 572024, China⁶ State Key Laboratory of Silicate Materials for Architectures, Wuhan University of Technology, Wuhan 430070, China

* Correspondence: pierluct@whut.edu.cn (P.-L.T.); tzhang@whut.edu.cn (T.Z.)

† These authors contributed equally to this work.

Abstract: Adsorption is a low-energy, economical, and efficient method for pollutant removal from water. Because of their unique structure, large specific surface area (SSA), and non-toxicity, bismuth-based semiconductors, usually researched for the photodegradation of organic molecules, are also excellent for dark adsorption processes. Here, a three-dimensional adsorbent with a heterostructure with a hydrangea-like shape made of Bi₂MoO₆ (BMO) and BiOI (BOI) was synthesized by a one-pot solvothermal process and investigated for the adsorption of toxic dyes. BOI/BMO with an I-to-Mo ratio of 2.0 adsorbed 98.9% of the model pollutant rhodamine B (RhB) within 5 min with a maximum adsorption capacity of 72.72 mg/g in the dark at room temperature. When compared to pure BMO, the BOI₂/BMO heterostructure was 14.1 times more performant because of its flower-like morphology with multiple planes, an SSA that was 1.6-fold larger, increased porosity, the formation of heterojunctions, and a negative surface charge attracting RhB. Further investigation indicated that adsorption by BOI₂/BMO fitted the pseudo-second-order kinetic and the Langmuir isotherm models. In addition, the thermodynamic analysis showed that it was a spontaneous exothermic process probably relying on physisorption. Thus, the BOI/BMO adsorbent developed here is promising for the fast removal of toxic dyes from industrial wastewater.

Keywords: BiOI/Bi₂MoO₆; heterostructure; rhodamine B; dark adsorption; kinetics; thermodynamic

Citation: Onyedika, T.E.; Xu, M.; Deng, Y.; Liu, Y.; Li, L.; Tremblay, P.-L.; Zhang, T. The Quick Removal of Toxic Dye Molecules by an Efficient Adsorptive BiOI/Bi₂MoO₆ Heterostructure. *Catalysts* **2023**, *13*, 457. <https://doi.org/10.3390/catal13030457>

Academic Editors: Ileana Daniela Lick and Paula Osorio-Vargas

Received: 2 January 2023

Revised: 17 February 2023

Accepted: 20 February 2023

Published: 21 February 2023



Copyright: © 2023 by the authors. Licensee MDPI, Basel, Switzerland. This article is an open access article distributed under the terms and conditions of the Creative Commons Attribution (CC BY) license (<https://creativecommons.org/licenses/by/4.0/>).

1. Introduction

Water resources are vulnerable to organic dye contaminants released by the printing, textile, leather, and paper industries [1]. As much as 17% to 20% of all hydrosphere pollution comes from industrial dyes [2]. One of these dyes, rhodamine B (RhB), is a widely employed xanthene that damages ecosystems because of its high solubility and stability, poor biodegradability, as well as a lasting effect on aquatic life [3–5]. In addition, RhB is suspected to be cardiotoxic, mutagenic, and carcinogenic for humans [6,7]. Other examples of problematic dyes often found in wastewater include the azobenzene derivative methyl orange (MO) and the thiazine methylene blue (MB), both of which impact negatively human health as well as aquatic flora and fauna [8,9].

Traditional wastewater treatments including filtration, flocculation, aeration, and sedimentation are somewhat efficient for the removal of RhB and other dyes [10]. However, these techniques suffer from limitations such as secondary pollution, high cost and energy requirement, and insufficient quality of the water effluent. For these reasons, advanced

approaches and materials are being researched to eliminate aqueous dye pollution in a cost-effective manner. This includes the development of systems for the photocatalytic oxidation, biodegradation, chemical coagulation, and adsorption of dyes [11–18]. Among these, adsorption is widely investigated because of its simplicity, low energy consumption, high efficiency, biocompatibility, and tolerance to toxic molecules [19]. It is also easy to operate and functional over a wide range of pH and other environmental parameters [20].

In the field of pollutant removal, Bi-based semiconductors are mostly studied for the photocatalytic degradation of toxic molecules [7,11,21,22]. Because of their large specific surface area (SSA), non-toxicity, and unique structure, these materials are now also getting developed as dark adsorbents. This includes the adsorption of dyes and metals by BiOBr, BiOCl, Bi₂MoO₆ (BMO), Bi₂WO₆, BiVO₄, and BiO₂CO₃ [23–27].

BMO and the Bi oxyhalides BiOBr and BiOCl have been combined for adsorption processes, mainly because stable heterostructures have an increased SSA, resulting in a larger number of contact sites with pollutants compared to homostructures [22,27,28]. BMO is an Aurivillius oxide made of MoO₄^{2−} slabs interspaced with [Bi₂O₂]²⁺ layers [29,30]. This n-type semiconductor has a narrow energy bandgap (E_g), good stability, and is environmentally friendly, which is why it is a good candidate for catalyzing visible-light-driven pollutant oxidation [31,32]. In addition, BMO has a large SSA, and its surface is permeable [33]. These properties make BMO suitable for adsorption processes [22,34].

A third Bi oxyhalide, BiOI (BOI), has also been coupled with BMO and the resulting heterostructure has been investigated for the photocatalytic degradation of organic pollutants, but never for dark adsorption [33]. BOI is a ternary V-VI-VII semiconductor where [Bi₂O₂]²⁺ layers alternate with I[−] layers [35]. In this tetragonal structure, the Bi and O elements in the [Bi₂O₂]²⁺ layer are attached covalently while the I[−] ions form Van der Waals bonds with [Bi₂O₂]²⁺ [35]. Like BMO, BOI has a narrow E_g and can absorb a large part of the visible light spectrum, which is excellent for photocatalytic applications [33]. BOI is also known to have a high adsorptive capacity, which is related to its suitable SSA and porosity [36,37]. Furthermore, the synthesis method of BOI can be adjusted to obtain three-dimensional flower-like structures with an expanded surface maximizing interaction with pollutants [38].

In this work, we investigated the dark adsorption capacity of a BOI/BMO composite for the removal of RhB and other dyes from water. After its synthesis via a one-pot solvothermal method, the composition, surface, and morphology of the heterostructure were characterized by different spectroscopic and microscopic techniques. The performance and stability of BOI/BMO particles with varying fractions of both semiconductors were then evaluated under different experimental conditions. Lastly, the adsorption properties of the composite were investigated via kinetics, isotherms, and thermodynamic modeling.

2. Results and Discussion

2.1. XRD, FTIR, and XPS Analyses

The crystal structure of BOI/BMO with different I:Mo molar ratios was evaluated by X-ray diffraction (XRD) spectroscopy (Figure 1a). For pure BMO, the diffraction peaks observed at $2\theta = 28.3^\circ, 32.5^\circ, 46.7^\circ, 55.44^\circ,$ and 58.4° correspond to the (131), (002), (202), (331), and (262) crystal planes of Bi₂MoO₆ (JCPDS nos. 76-2388). For BOI₁/BMO with a I:Mo ratio of 1.0, no other peak was detected besides the ones associated with BMO. When the I doping was increased to 2.0, an additional peak was observed at 31.7° . Further augmenting the I:Mo ratio to 3.0 resulted in four additional peaks appearing at $29.7^\circ, 31.7^\circ, 45.5^\circ,$ and 51.5° . These peaks are distinctive of the (012), (110), (020), and (114) crystal planes of the tetragonal phase of BiOI (JCPDS no. 73-2062) [39]. Thus, for BOI/BMO composites, all detected peaks were attributable to either BMO or BOI, indicating high purity. With an increase in the I/Mo molar ratio, the characteristic peak intensity of BMO gradually decreased, while that of BOI gradually increased, demonstrating the successful synthesis of BOI/BMO heterostructures by a one-pot solvothermal method. In addition, the crystallite size of BMO, BOI₁/BMO, BOI₂/BMO, and BOI₃/BMO, as determined by

Scherrer's equation [40], was 9.8 nm, 6.2 nm, 5.9 nm, and 6.4 nm, respectively. The difference in size between pure BMO and the heterostructure materials is probably due to the high dispersity and low crystallinity of BOI [41].

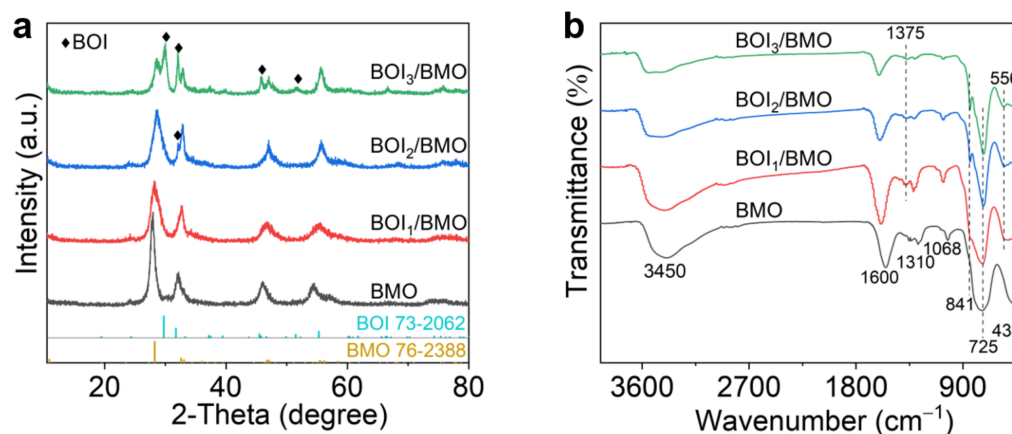


Figure 1. (a) XRD and (b) FTIR spectra of BMO, BOI₁/BMO, BOI₂/BMO, and BOI₃/BMO.

Fourier transform infrared (FTIR) spectra of pure BMO and BOI_{1–3}/BMO all exhibited broad bands at 3450 and 1600 cm^{−1} attributed to O-H groups from water molecules adsorbed on the surface (Figure 1b) [42]. Peaks in the 1000–1500 cm^{−1} range correspond to C=O and C-O from CO₂ impurities deposited on the catalyst [43,44]. The peak at 841 cm^{−1} originates from the asymmetric and symmetric stretchings of the apical oxygen atom in MoO₆ [45]. The characteristic band at 725 cm^{−1} corresponds to the bending and asymmetric stretching of Mo-O in the MoO₆ octahedron [46]. In BOI/BMO samples, this peak became sharper compared to pure BMO, indicating that the formation of BOI, after the addition of KI to the solvothermal synthesis process, reduced the asymmetric stretching vibration of the MoO₆ octahedron [44]. Peaks at 439 and 556 cm^{−1} further confirmed BOI formation and are assigned to Bi-O vibration and stretching mode, respectively [47,48]. Another band at 1375 cm^{−1} could be distinctive of asymmetric and symmetric stretching vibrations of Bi-I [49].

The X-ray photoelectron survey spectrum (XPS) shows binding energy peaks for Bi, Mo, O, and I elements on the surface of the BOI₂/BMO heterostructure (Figure S1). A C 1s peak is also present and was attributed to environmental contamination during sample analysis [50]. Based on the XPS results, the atomic percentages of Bi, Mo, O, and I were 22.03%, 5.68%, 67.66%, and 4.62%, respectively. Thus, the real fraction of I in the heterostructure is lower than what was actually fed to the reaction. This is consistent with other studies reporting that not all the added I molecules will react [11,51].

The I 3d high-resolution XPS spectrum of BOI₂/BMO exhibited two peaks for I 3d_{5/2} and I 3d_{3/2}, indicating that the I element existed in the form of I[−] (Figure 2a) [52,53]. The Bi 4f spectra of both pure BMO and BOI₂/BMO also had two peaks corresponding to Bi 4f_{5/2} and Bi 4f_{7/2} and confirming the presence of Bi³⁺ (Figure 2b). On the same spectra, two less prominent peaks with higher binding energy were observed for both pure BMO and BOI₂/BMO. These peaks are possibly related to small surface charge effect polarization changes in the crystal [54]. The Mo 3d spectra had two peaks corresponding to Mo 3d_{5/2} and Mo 3d_{3/2}, which are characteristic of Mo⁶⁺ species (Figure 2c). Both O 1s XPS spectra of BMO and BOI₂/BMO show an asymmetric peak that can be decomposed into three parts, indicating the presence of surface Bi-O, Mo-O/I-O, and O-H [55–57]. In addition, peaks on the Bi 4f, Mo 3d, and O 1s spectra of BOI₂/BMO shifted toward higher binding energy compared to pure BMO. This can be attributed to the formation of a built-in electric field at the interface of BOI and BMO and is another evidence of the successful formation of the heterostructure [33].

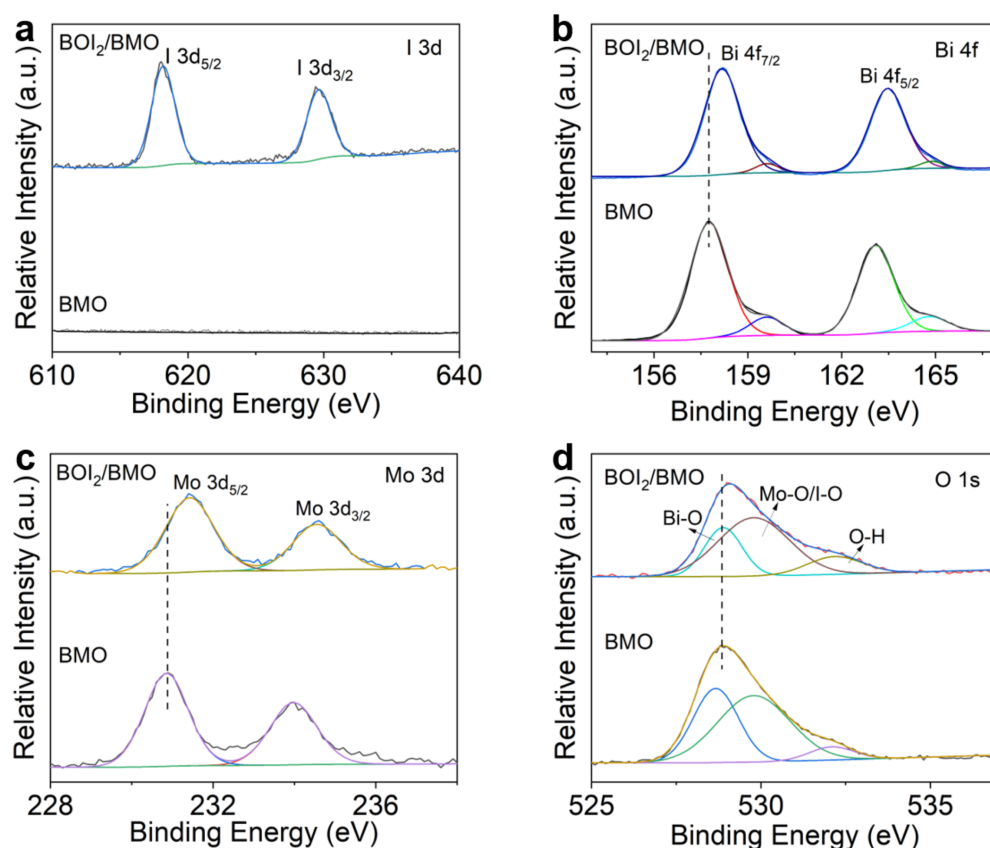


Figure 2. High-resolution XPS spectra of (a) I 3d, (b) Bi 4f, (c) Mo 3d, and (d) O 1s for BMO and BOI₂/BMO.

2.2. Morphology and Surface Characterization

The scanning electron micrograph (SEM) of pure BMO shows a large sphere made of aggregated nanosheets (Figure 3a). When BOI was added, the heterostructure became a three-dimensional hydrangea-like shape with more exposed planes (Figure 3b). In addition, BOI₂/BMO spheres were significantly smaller. Compared to pure BMO, the shape and size of BOI₂/BMO are more suitable for dark adsorption processes by providing a larger number of binding sites for the pollutant molecules [42,44]. Transmission electron microscopy (TEM) supported these results and showed that BOI₂/BMO had a narrower shape with an outline that was irregular compared to pure BMO (Figure S2). In addition, high-resolution TEM (HRTEM) micrographs of both pure BMO and BOI₂/BMO exhibited a spacing of 0.32 nm, corresponding to the (131) crystal plane of BMO. BOI₂/BMO also had a spacing of 0.30 nm, which is distinctive of the (012) crystal plane of BOI, further confirming the synthesis of the heterojunction adsorbent.

Next, a Brunauer–Emmett–Teller (BET) analysis was conducted to gain more insights into the surface of the heterostructure (Figure 3c,d). Both pure BMO and BOI₂/BMO displayed type (IV) isotherms with a H₃ hysteresis loop indicative of a mesoporous structure (Figure 3c). In agreement with its morphology and smaller size, the SSA of BOI₂/BMO was larger at 68.6 m²/g compared to 41.9 m²/g for pure BMO. BOI₂/BMO also had bigger pores with an average diameter of 18.2 nm and a total pore volume of 0.31 cm³/g (Figure 3d). In comparison, the average pore diameter and total pore volume of pure BMO were 15.7 nm and 0.16 cm³/g, respectively. The bigger SSA and pore volume of BOI₂/BMO are beneficial for adsorption as they increase available active sites and facilitate the rapid transfer of adsorbate molecules [58].

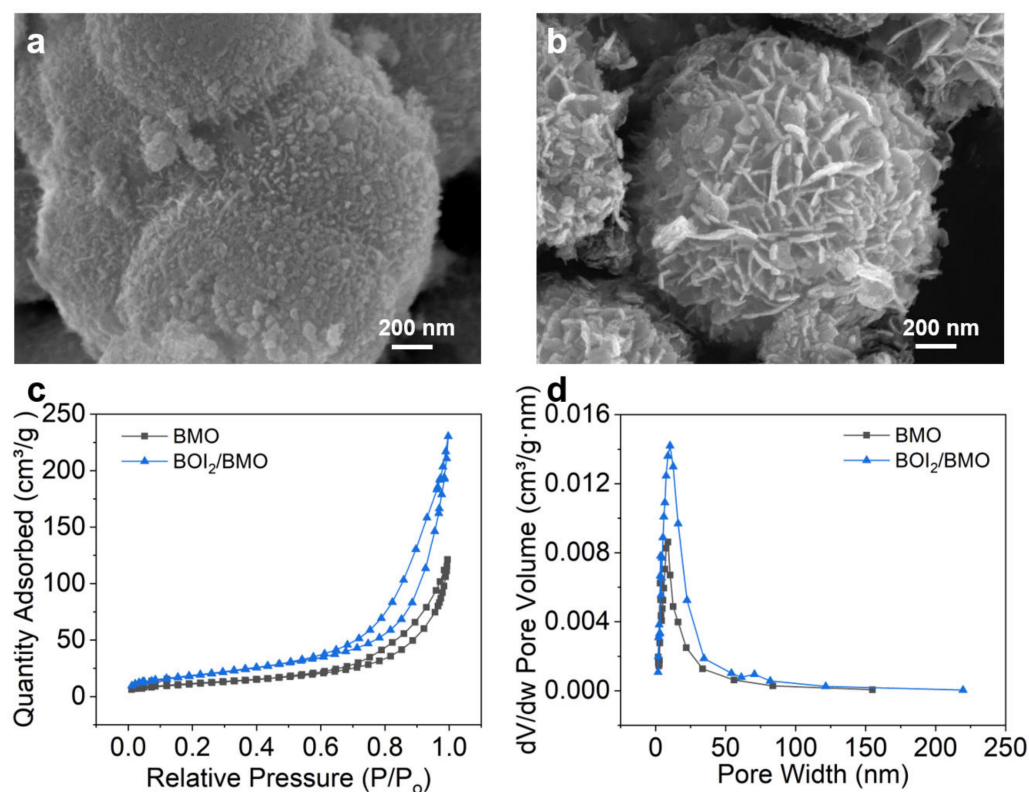


Figure 3. SEM micrographs of (a) BMO and (b) BOI₂/BMO. (c) N₂ adsorption–desorption isotherms and (d) pore size distribution curves.

2.3. Toxic Dyes Adsorption Performance by BOI/BMO

BOI/BMO composites with different I:Mo molar ratios (0.1, 0.2, 0.4, 0.6, 0.8, 1.0, 1.6, 2.0, 2.6, and 3.0) were evaluated for the removal in the dark of the widely used toxic dye RhB (Figure 4a,b). This experiment was conducted with 50 mg adsorbent in a 10 mg/L RhB solution with an unadjusted pH of 4.8. The most performant heterostructure had a I:Mo ratio of 2.0 and adsorbed 98.9% RhB after only 5 min. This excellent adsorption rate was 14.1 times higher than pure BMO (7.0%) and 2.3 times higher than pure BOI (43.4%). BOI₂/BMO was also faster than many BMO heterojunction-based adsorption systems for RhB (Table 1). Besides SSA and porosity, another major factor responsible for the higher adsorption capacity of the heterostructure was its surface charge. While the zeta potential of pure BMO was 12 mV, BOI₂/BMO exhibited a negative potential of −4.0 mV because of the abundance of I[−] anions on its surface. Thus, the composite was more suitable for the electrostatic attraction of cationic RhB molecules.

Table 1. Examples of RhB adsorption performance by Bi₂MoO₆-based materials.

Absorbent	Time (min)	Removal Efficiency (%)	Adsorbent Dosage (mg)	[RhB] (mg/L)	Reaction Volume (mL)	Reference
BiOBr/Bi ₂ MoO ₆	120	98.4 ^a	20	30	20	[22]
Bi ₂ MoO ₆ @BiOCl@MOF-199	10	30.0 ^b	100	7.5	200	[24]
MnFe ₂ O ₄ /Bi ₂ MoO ₆ /PPy	120	54.9 ^b	30	10	50	[59]
Bi ₂ MoO ₆ @BiOCl	8	94.0 ^b	100	7	200	[27]
BiOI/Bi ₂ MoO ₆ (BOI ₂ /BMO)	5	98.9 ^b	50	10	50	This work

^a The reaction pH was adjusted to 2. ^b The reaction pH was not adjusted.

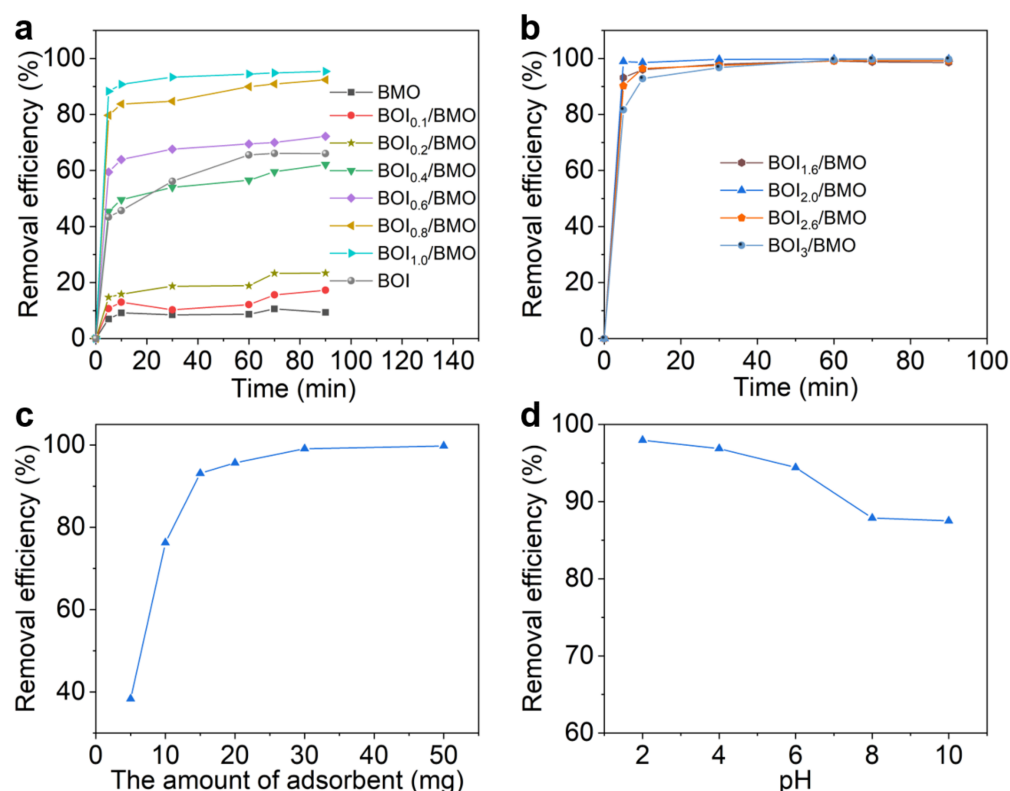


Figure 4. Dark adsorption of RhB (10 mg/L) by (a) BMO, BOI, BOI_{0.1-1.0}/BMO, and (b) BOI_{1.6-3.0}/BMO (50 mg) over time. Effect of (c) adsorbent quantity and (d) pH on RhB removal by BOI₂/BMO.

When the I:Mo ratio was above 2.0, the performance of the heterostructure adsorbent declined (Figure 4b). For instance, BOI₃/BMO removed 81.6% RhB after 5 min. This demonstrates the central role of heterojunctions between BMO and BOI for the adsorption process. As the BOI content increased up to I:Mo = 2, more interfaces were formed between BOI and BMO. However, when the BOI content was higher than the optimal value, efficient heterojunctions between the two semiconductors probably plateaued while BOI in excess started interfering with efficient RhB removal.

Different adsorbent quantities and reaction pHs were then screened to identify optimal RhB removal conditions (Figure 4c,d). From 5 to 15 mg BOI₂/BMO, adsorption rates increased significantly (Figure 4c). From 15 to 30 mg BOI₂/BMO, adsorption rates still augmented, but slower. For instance, 15 mg and 20 mg adsorbent removed 93.1% and 95.9% RhB after 90 min, respectively. At higher BOI₂/BMO concentrations, adsorption rates nearly plateaued. For this reason, 20 mg adsorbent was chosen to perform the subsequent kinetics, isotherms, and thermodynamic analyses. Next, 20 mg BOI₂/BMO was tested at pHs ranging from 2 to 10 (Figure 4d). The adsorption performance was optimal at the most acidic pH of 2 with a RhB removal of 98.0% after 90 min. At more basic pH values, the adsorbent lost efficiency with the lowest RhB removal of 87.5% recorded at pH 10. This observation mainly related to the electronic status of RhB at different pH. When the pH is below 4, RhB cations are mostly monomers in the solution that will be attracted by negatively charged BOI₂/BMO and entered its pores. When the pH is above 4, RhB exists mainly as a zwitterion, which weakens its positive charge and makes it more likely to polymerize and less likely to interact with the surface of the adsorbent [60,61].

Besides RhB, the optimal adsorbent BOI₂/BMO was also evaluated for the removal of two other toxic dyes, MO and MB (Figure S3). After 5 min, BOI₂/BMO adsorbed 49.1% MO and 68.1% MB. The equilibrium was reached after 30 min with the adsorption of 59.1% and 85.0% of MO and MB, respectively. These results show that BOI₂/BMO can adsorb other industrial dyes than RhB, although not as efficiently.

2.4. Adsorption Kinetics and Isotherms

The dark adsorption of RhB by 20 mg BOI₂/BMO over time is presented in Figure 5a.

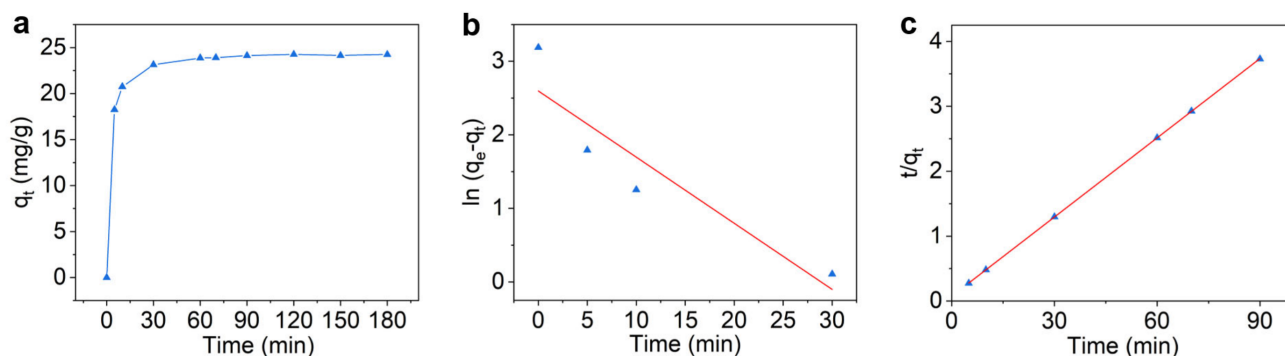


Figure 5. (a) Time-dependent RhB (10 mg/L) adsorption by 20 mg BOI₂/BMO. (b) Pseudo-first-order kinetics and (c) pseudo-second-order kinetics plots.

In the first 5 min, RhB was rapidly removed from the aqueous solution with an adsorption capacity at this specific time (q_t) of 18.25 mg/g. Then, the adsorption rate decreased gradually and the equilibrium (q_e) was reached after 60 min (23.90 mg/g). At time 0, there is a large number of active adsorption sites available for the capture of RhB on the unique surface of BOI₂/BMO. Later, adsorption sites become occupied and the little number of RhB molecules remaining in solution are less likely to encounter a free one and be removed quickly.

The kinetics data were then integrated into the pseudo-first-order and pseudo-second-order models to further understand the adsorption mechanism responsible for RhB removal by BOI₂/BMO (Figure 5b,c). The equation (Equation (1)) for the linearized pseudo-first-order model is:

$$\ln(q_e - q_t) = \ln q_e - k_1 t \quad (1)$$

where k_1 is the rate constant (min^{-1}) and t is the time [62].

The next Equation (2) was employed to calculate the linearized pseudo-second-order model:

$$t/q_t = 1/(k_2 q_e^2) + t/q_e \quad (2)$$

where k_2 is the rate constant (g/mg/min) [63].

The results clearly showed that BOI₂/BMO adsorbed RhB according to the pseudo-second-order kinetics model with an excellent R^2 of 0.999, a k_2 of 0.022 g/mg/min, and a theoretical q_e of 24.58 mg/g close to the experimental one (Figure 5b,c, Table S1) [64,65].

The impact of the toxic dye's initial concentration and the temperature on the adsorption process by BOI₂/BMO were then investigated (Figure 6). With the increase in RhB concentration, the q_e values augmented (Figure 6a). This is mainly because the diffusion rate of RhB at higher initial concentrations into BOI₂/BMO was faster and the concentration gradient force gained in strength [62]. In the case of temperature, BOI₂/BMO became less efficient with lower q_e values at 308 and 318 K compared to 298 K (Figure 6a). This tendency indicates that RhB absorption by the heterostructure is an exothermic process more performant at lower temperatures.

Data from the isothermal adsorption study were then fitted in the linearized Langmuir (Equations (3) and (4)) and Freundlich (Equation (5)) isotherm models to explore further the adsorption mechanism and calculate the theoretical maximum adsorption capacity (q_m) according to the following equations (Figure 6b,c):

$$c_e/q_e = 1/(K_L q_m) + c_e/q_m \quad (3)$$

where c_e is the concentration of RhB at equilibrium and K_L (L/mg) is the adsorption equilibrium constant of the Langmuir model.

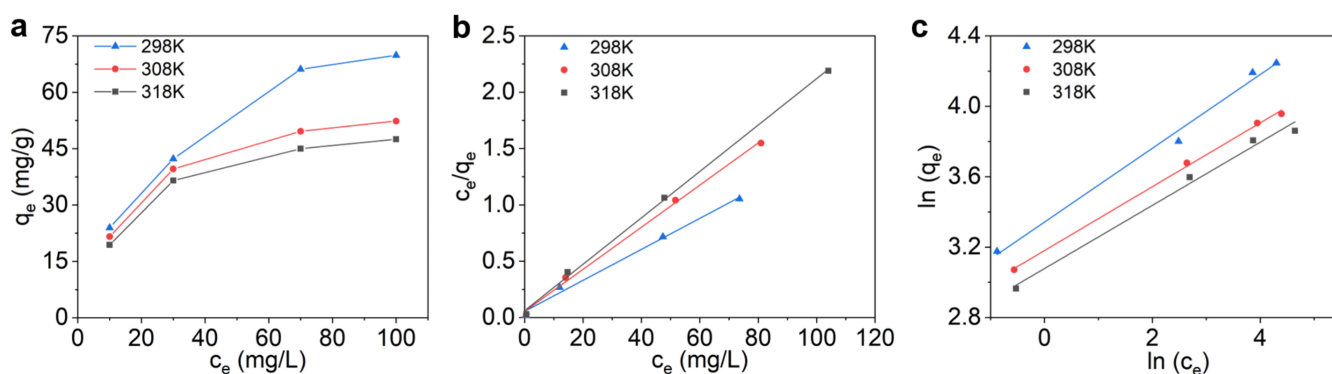


Figure 6. (a) The adsorption of different RhB concentrations by 20 mg BOI₂/BMO at 298, 308, and 318 K. Linear (b) Langmuir and (c) Freundlich isotherm model plots.

The dimensionless separation constant R_L was also calculated based on the Langmuir isotherm model to predict whether the adsorption reaction by BOI₂/BMO was favorable or not:

$$R_L = 1/(1 + K_L c_0) \quad (4)$$

where c_0 is the initial RhB concentration.

The Freundlich adsorption isotherm model equation is:

$$\ln q_e = \ln K_F + (1/n) \ln c_e \quad (5)$$

where K_F (L/mg) and n are empirical constants.

The R^2 values from these mathematical models indicated that the adsorption process fitted better with the linearized Langmuir isotherm, which means that RhB molecules bound to sites homogeneously distributed onto a monolayer (Figure 6b,c, Table S2) [66]. Based on this model, the theoretical q_m of BOI₂/BMO for RhB at room temperature was 72.72 mg/g. At all the tested temperatures, R_L values (0.028~0.039) derived from the Langmuir isotherm were between 0 to 1. This indicates that RhB adsorption by BOI₂/BMO is a favorable process [67,68].

2.5. Thermodynamic Analysis

To better understand the adsorption of RhB by BOI₂/BMO, thermodynamic parameters including standard free energy change (ΔG°), standard enthalpy change (ΔH°), and standard entropy change (ΔS°) were calculated according to the following equations [69]:

$$\Delta G^\circ = -RT \ln b \quad (6)$$

$$\Delta H^\circ = -RT_2 T_1/T_2 - T_1 \ln (b_2/b_1) \quad (7)$$

$$\Delta S^\circ = \Delta H^\circ - \Delta G^\circ/T \quad (8)$$

where R is the universal gas constant, T is the absolute temperature (K), and b is the Langmuir adsorption constant (K_L converted in mg/g) at different temperatures T .

The calculated thermodynamic parameters are presented in Table 2. ΔG° values were below 0 and changed very little with temperature variation, indicating that the RhB adsorption reaction was spontaneous. The ΔH° average value of -11.53 kJ/mol was negative further confirming the exothermic nature of RhB capture by BOI₂/BMO and indicating that physisorption was probably the mechanism involved [70]. In general, it is assumed that adsorption ΔH° in the -20 to 40 kJ/mol range are indicative of physisorption [71]. The ΔS° values were positive at all three tested temperatures showing that the randomness at the interface between the adsorbent and the aqueous solution containing RhB molecules augmented and thus strongly suggesting structural changes in the toxic dye and BOI₂/BMO during adsorption [72].

Table 2. Thermodynamic parameters for RhB adsorption by BOI₂/BMO.

Temperature (K)	ΔG^0 (kJ/mol)	ΔS^0 (J/mol/K)	ΔH^0 (kJ/mol)
298	−30.78	64.60	
308	−32.62	68.47	−11.53 ^a
318	−33.64	69.53	

^a ΔH^0 value is the average of enthalpy changes.

2.6. The Stability of BOI₂/BMO

Next, a cycling experiment was conducted where the heterostructure adsorbent was reused multiple times to assess its long-term stability (Figure S4). Following RhB adsorption, BOI₂/BMO was extensively washed three times with anhydrous ethanol and ultrapure water, dried in an oven at 55 °C for 6 h before being recycled. After five cycles, BOI₂/BMO remained capable of removing 90.8% of RhB molecules, showing good stability. In addition, an SEM image indicated that the hydrangea-like structure of the heterojunction adsorbent was mostly preserved.

3. Materials and Methods

3.1. Materials

Na₂MoO₄·2H₂O was purchased from Yuanye Bio-Technology (Shanghai, China) and Bi(NO₃)₃·5H₂O was acquired from Aladdin Chemical Reagent (Shanghai, China). Ethylene glycol, anhydrous ethanol, KI, RhB, and MB were purchased from Sinopharm Chemical Reagent (Shanghai, China). MO was obtained from Macklin Biochemical (Shanghai, China). All reagents were analytical grade and were used without further treatment.

3.2. Synthesis of Pure Bi₂MoO₆, BiOI, and Heterostructure BiOI/Bi₂MoO₆

For pure BMO synthesis, 0.325 mmol Na₂MoO₄·2H₂O and 0.65 mmol Bi(NO₃)₃·5H₂O were separately dissolved in 6 mL ethylene glycol. These two solutions were mixed and stirred at 500 rpm for 30 min at room temperature. Then, 30 mL anhydrous ethanol was added to the reaction followed by stirring for an additional 2 h. For the BOI/BMO composites, various concentrations of KI were added at this step. The mixture was transferred to a Teflon-lined autoclave and reacted at 160 °C for 24 h. The resulting solid was then washed three times with distilled water and anhydrous ethanol. Lastly, the product was dried in an oven at 55 °C for 12 h before being ground into a fine powder. The composites were labeled as BOI_x/BMO where x is the I:Mo molar ratio. Pure BOI was synthesized in a similar manner to BOI/BMO, but Na₂MoO₄·2H₂O was omitted from the first step.

3.3. Composition, Structure, and Morphology Characterization

The XRD analysis was performed with a D8 Advance X-ray diffractometer (Bruker, Billerica, Germany) in the 10–80° range with Cu K α as the radiation source. The FTIR spectroscopy was done with a Nicolet iS5 spectrometer (Thermo Fisher Scientific, Waltham, MA, USA) in the 4000–400 cm^{−1} range with a KBr base. The surface of the samples was studied with an ESCALAB 250 Xi X-ray photoelectron spectrometer (Thermo Fisher Scientific) with Al K α radiation. SEM micrographs were taken with a Phenom Pharos G2 field-emission-gun-SEM system (Thermo Fisher Scientific) at an accelerating voltage of 15 kV. TEM and HRTEM images were obtained with a JEM-2100F field emission electron microscope (JEOL, Tokyo, Japan) at an accelerating voltage of 200 kV. The BET analysis was carried out with an ASAP 2460 surface area and porosimetry analyzer (Micromeritics, Norcross, GA, USA). The zeta potential of the samples was recorded with a Nano-ZS ZEN 3600 Zetasizer instrument (Malvern Panalytical, Malvern, UK).

3.4. Adsorption of RhB and Other Dyes by the Bi-Based Adsorbents

In a typical experiment, 50 mg of the adsorbent material was added to 50 mL of an aqueous solution containing 10 mg/L of toxic dyes. The reaction was then stirred

at 300 rpm for 90 min at 25 °C in the dark. To measure the remaining concentration of toxic dyes in solution, the adsorption reaction was centrifuged at $10,000\times g$ for 5 min at room temperature. The remaining RhB, MO, or MB concentration in the supernatant was measured with an Evolution 220 UV-Visible spectrophotometer (Thermo Fisher Scientific) at 554 nm, 464 nm, and 662 nm, respectively, as previously described [73–75]. Where indicated, the quantity of adsorbent added to the reaction was varied between 5 to 50 mg, the pH of the adsorbate solution was adjusted at values ranging from 2 to 10 with 1 M NaOH and HCl, the initial concentration of RhB was changed from 10 to 100 mg/L, the reaction time was extended to 180 min, or the temperature was set at 35 °C (308 K) or 45 °C (318 K).

4. Conclusions

The BOI/BMO catalyst prepared with an I:Mo ratio of 2.0 by a one-pot solvothermal synthesis method was the most efficient for the fast removal of toxic RhB by dark adsorption. It could remove nearly all RhB molecules within 5 min and exhibited a good q_m of 72.72 mg/g at room temperature. BOI₂/BMO also adsorbed other dyes besides RhB, but not as efficiently. Its hydrangea-like morphology, large SSA and pore volume, negative surface charge, as well as heterojunction between two semiconductors are all factors contributing to the superior BOI/BMO adsorption performance compared to pure BMO, BOI, and other Bi-based adsorbents reported in the literature (Table 1). In summary, BOI/BMO is a low-cost and environmentally friendly adsorbent showing great potential for practical application in the field of water treatment.

Supplementary Materials: The following supporting information can be downloaded at: <https://www.mdpi.com/article/10.3390/catal13030457/s1>, Figure S1: XPS survey spectra for BMO and BOI₂/BMO; Figure S2: TEM and HRTEM micrographs of BMO and BOI₂/BMO; Figure S3: Adsorption of MO and MB by BOI₂/BMO; Figure S4: Stability of BOI₂/BMO after multiple reuses; Table S1: Parameters for kinetic models of RhB adsorption by BOI₂/BMO; Table S2: Parameters for isotherms models of RhB adsorption by BOI₂/BMO.

Author Contributions: T.E.O.: Investigation, Methodology, Writing—original draft. M.X.: Investigation, Methodology, Formal analysis, Data curation, Software, Visualization, Writing—review and editing, Funding acquisition. Y.D.: Investigation, Methodology. Y.L.: Investigation, Methodology. L.L.L.: Writing—original draft. P.-L.T.: Conceptualization, Formal analysis, Visualization, Writing—review and editing, Funding acquisition. T.Z.: Conceptualization, Project administration, Funding acquisition, Resources, Supervision, Writing—review and editing. All authors have read and agreed to the published version of the manuscript.

Funding: This study was funded by Wuhan University of Technology, the Shaoxing 330 overseas elites Plan, and the National Natural Science Foundation of China (No. 52102110).

Data Availability Statement: All the data generated during this work are included in this published article and its Supplementary Materials. Additional data are available from the corresponding authors.

Conflicts of Interest: The authors declare no conflict of interest. Mengying Xu will be employed by Zhejiang Xingguang Pharmaceutical Co., Ltd. between 8 November 2022 and 28 October 2024. No support, financial or otherwise, has been received from this company that may influence the submitted work.

References

1. Zhao, G.Y.; Liu, L.J.; Li, J.R.; Liu, Q. Efficient removal of dye MB: Through the combined action of adsorption and photodegradation from NiFe₂O₄/Ag₃PO₄. *J. Alloys Compd.* **2016**, *664*, 169–174. [CrossRef]
2. Kant, R. Textile dyeing industry an environmental hazard. *Nat. Sci.* **2012**, *4*, 22–26. [CrossRef]
3. Solís, M.; Solís, A.; Pérez, H.I.; Manjarrez, N.; Flores, M. Microbial decolouration of azo dyes: A review. *Process Biochem.* **2012**, *47*, 1723–1748. [CrossRef]
4. Kropf, C.; Segner, H.; Fent, K. ABC transporters and xenobiotic defense systems in early life stages of rainbow trout (*Oncorhynchus mykiss*). *Comp. Biochem. Physiol. C Toxicol. Pharmacol.* **2016**, *185–186*, 45–56. [CrossRef]

5. Mohanty, L.; Sundar Pattanayak, D.; Singhal, R.; Pradhan, D.; Kumar Dash, S. Enhanced photocatalytic degradation of rhodamine B and malachite green employing BiFeO₃/g-C₃N₄ nanocomposites: An efficient visible-light photocatalyst. *Inorg. Chem. Commun.* **2022**, *138*, 109286. [[CrossRef](#)]
6. Rafique, M.A.; Jamal, A.; Afzal, G.; Abrar, S.; Kiran, S.; Nosheen, S.; Hussain, H.M.H.; Majeed, T. Photocatalytic mediated remediation of synthetic dyes effluent using zero-valent iron: A comparative study. *Desalin. Water Treat.* **2021**, *237*, 284–291. [[CrossRef](#)]
7. Xu, M.Y.; Deng, Y.C.; Li, S.H.; Zheng, J.Y.; Liu, J.Y.; Tremblay, P.L.; Zhang, T. Bacterial cellulose flakes loaded with Bi₂MoO₆ nanoparticles and quantum dots for the photodegradation of antibiotic and dye pollutants. *Chemosphere* **2023**, *312*, 137249. [[CrossRef](#)] [[PubMed](#)]
8. Sivakumar, R.; Lee, N.Y. Adsorptive removal of organic pollutant methylene blue using polysaccharide-based composite hydrogels. *Chemosphere* **2022**, *286*, 131890. [[CrossRef](#)] [[PubMed](#)]
9. Iwuozor, K.O.; Ighalo, J.O.; Emenike, E.C.; Ogunfowora, L.A.; Igwegbe, C.A. Adsorption of methyl orange: A review on adsorbent performance. *Curr. Res. Green Sustain. Chem.* **2021**, *4*, 100179. [[CrossRef](#)]
10. Al-Gheethi, A.A.; Azhar, Q.M.; Senthil Kumar, P.; Yusuf, A.A.; Al-Buriahi, A.K.; Radin Mohamed, R.M.S.; Al-Shaibani, M.M. Sustainable approaches for removing Rhodamine B dye using agricultural waste adsorbents: A review. *Chemosphere* **2022**, *287*, 132080. [[CrossRef](#)]
11. Deng, Y.C.; Xu, M.Y.; Jiang, X.Y.; Wang, J.T.; Tremblay, P.L.; Zhang, T. Versatile iodine-doped BiOCl with abundant oxygen vacancies and (110) crystal planes for enhanced pollutant photodegradation. *Environ. Res.* **2023**, *216*, 114808. [[CrossRef](#)]
12. Saravanan, S.; Carolin, C.F.; Kumar, P.S.; Chitra, B.; Rangasamy, G. Biodegradation of textile dye Rhodamine-B by *Brevundimonas diminuta* and screening of their breakdown metabolites. *Chemosphere* **2022**, *308*, 136266. [[CrossRef](#)] [[PubMed](#)]
13. Zhu, X.B.; Zhang, J.L.; Wu, S.Y.; Zhou, Z.C. Efficient coagulation and removal of aqueous graphene oxide by different dyes. *Desalin. Water Treat.* **2021**, *217*, 339–349. [[CrossRef](#)]
14. Yen Doan, T.H.; Minh Chu, T.P.; Dinh, T.D.; Nguyen, T.H.; Tu Vo, T.C.; Nguyen, N.M.; Nguyen, B.H.; Nguyen, T.A.; Pham, T.D. Adsorptive removal of rhodamine B using novel adsorbent-based surfactant-modified alpha alumina nanoparticles. *J. Anal. Methods Chem.* **2020**, *2020*, 6676320. [[CrossRef](#)]
15. Du, H.L.; Zhang, Y.S.; Jiang, H.R.; Wang, H. Adsorption of rhodamine B on polyvinyl chloride, polystyrene, and polyethylene terephthalate microplastics in aqueous environments. *Environ. Technol. Innov.* **2022**, *27*, 102495. [[CrossRef](#)]
16. Singh, A.; Singh, A.K.; Liu, J.; Kumar, A. Syntheses, design strategies, and photocatalytic charge dynamics of metal–organic frameworks (MOFs): A catalyzed photo-degradation approach towards organic dyes. *Catal. Sci. Technol.* **2021**, *11*, 3946–3989. [[CrossRef](#)]
17. Dong, X.; Li, Y.; Li, D.; Liao, D.; Qin, T.; Prakash, O.; Kumar, A.; Liu, J. A new 3D 8-connected Cd(II) MOF as a potent photocatalyst for oxytetracycline antibiotic degradation. *CrystEngComm* **2022**, *24*, 6933–6943. [[CrossRef](#)]
18. Zheng, M.; Chen, J.; Zhang, L.; Cheng, Y.; Lu, C.; Liu, Y.; Singh, A.; Trivedi, M.; Kumar, A.; Liu, J. Metal organic frameworks as efficient adsorbents for drugs from wastewater. *Mater. Today Commun.* **2022**, *31*, 103514.
19. Du, X.C.; Zhu, J.H.; Quan, Z.J.; Wang, X.C. Adsorption of rhodamine B by organic porous materials rich in nitrogen, oxygen, and sulfur heteroatoms. *New J. Chem.* **2021**, *45*, 3448–3453. [[CrossRef](#)]
20. Wang, X.H.; Chen, S.Q.; Sun, J.C.; Zhang, D.H.; Yan, Z.H.; Xu, X.Y.; Song, J.Q. Synthesis of large pore sized mesoporous carbon using alumina-templated strategy for high-performance RhB removal. *Microporous Mesoporous Mater.* **2021**, *318*, 110993. [[CrossRef](#)]
21. Li, R.Z.; Chen, H.Y.; Xiong, J.R.; Xu, X.Y.; Cheng, J.J.; Liu, X.Y.; Liu, G. A mini review on bismuth-based z-scheme photocatalysts. *Materials* **2020**, *13*, 5057. [[CrossRef](#)]
22. Wang, D.J.; Shen, H.D.; Guo, L.; Wang, C.; Fu, F. Porous BiOBr/Bi₂MoO₆ heterostructures for highly selective adsorption of methylene blue. *ACS Omega* **2016**, *1*, 566–577. [[CrossRef](#)]
23. Yang, H.Y.; Zhao, S.Q.; Zhuang, X.J.; Asuha, S. Hydrothermal synthesis of Bi₂WO₆/mesoporous TiO₂ nanocomposites and their adsorptive properties. *J. Nanopart. Res.* **2022**, *24*, 159. [[CrossRef](#)]
24. Shah, A.H.; Yuan, C.; Hao, W.Y.; Gu, W.H.; Liang, S.Y.; Abideen, Z.U.; Wahid, F.; Teng, F. Adsorption kinetics of simulated mixture wastewaters over porous Bi₂MoO₆@BiOCl@MOF-199 heterostructure. *J. Solid State Chem.* **2022**, *307*, 122835. [[CrossRef](#)]
25. Kong, D.F.; Li, W.J.; Yan, T.J.; Wang, Z.; Kong, D.S.; You, J.M. Preparation of novel BiVO₄ nanofibers and their excellent adsorptive properties. *Mater. Res. Bull.* **2018**, *105*, 84–90. [[CrossRef](#)]
26. Liu, H.J.; Chen, M.; Wei, D.D.; Ma, Y.Q.; Wang, F.L.; Zhang, Q.X.; Shi, J.L.; Zhang, H.; Peng, J.B.; Liu, G.G.; et al. Smart removal of dye pollutants via dark adsorption and light desorption at recyclable Bi₂O₂CO₃ nanosheets interface. *ACS Appl. Mater. Interfaces* **2020**, *12*, 20490–20499. [[CrossRef](#)] [[PubMed](#)]
27. Shah, A.H.; Gu, W.H.; Abideen, Z.U.; Teng, F. Removal of chromium from aqueous solution by porous Bi₂MoO₆@BiOCl nanostructure. *J. Solid State Chem.* **2020**, *292*, 121719. [[CrossRef](#)]
28. Li, Y.; Wang, Z.; Huang, B.; Dai, Y.; Zhang, X.; Qin, X. Synthesis of BiOBr-PVP hybrids with enhanced adsorption-photocatalytic properties. *Appl. Surf. Sci.* **2015**, *347*, 258–264. [[CrossRef](#)]
29. Yu, H.B.; Jiang, L.B.; Wang, H.; Huang, B.B.; Yuan, X.Z.; Huang, J.H.; Zhang, J.; Zeng, G.M. Modulation of Bi₂MoO₆-based materials for photocatalytic water splitting and environmental application: A critical review. *Small* **2019**, *15*, 1901008. [[CrossRef](#)]

30. Yang, L.; Du, C.Y.; Tan, S.Y.; Zhang, Z.; Song, J.H.; Su, Y.H.; Zhang, Y.; Wang, S.T.; Yu, G.L.; Chen, H.; et al. Improved photocatalytic properties of Fe(III) ion doped Bi₂MoO₆ for the oxidation of organic pollutants. *Ceram. Int.* **2021**, *47*, 5786–5794. [[CrossRef](#)]
31. Di, J.; Xia, J.X.; Ji, M.X.; Li, H.P.; Xu, H.; Li, H.M.; Chen, R. The synergistic role of carbon quantum dots for the improved photocatalytic performance of Bi₂MoO₆. *Nanoscale* **2015**, *7*, 11433–11443. [[CrossRef](#)]
32. Li, S.J.; Liu, Y.P.; Long, Y.Q.; Mo, L.Y.; Zhang, H.Q.; Liu, J.S. Facile synthesis of Bi₂MoO₆ microspheres decorated by CdS nanoparticles with efficient photocatalytic removal of levofloxacin antibiotic. *Catalysts* **2018**, *8*, 477. [[CrossRef](#)]
33. Yan, T.; Sun, M.; Liu, H.Y.; Wu, T.T.; Liu, X.J.; Yan, Q.; Xu, W.G.; Du, B. Fabrication of hierarchical BiOI/Bi₂MoO₆ heterojunction for degradation of bisphenol A and dye under visible light irradiation. *J. Alloys Compd.* **2015**, *634*, 223–231. [[CrossRef](#)]
34. Matsuura, I.; Schuit, G.C.A. Adsorption and reaction of adsorbed species on Bi₂MoO₆ catalyst: Influence on sintering and of temperature of reduction. *J. Catal.* **1972**, *25*, 314–325. [[CrossRef](#)]
35. Zhou, G.L.; Tian, Z.X.; Sun, H.G.; Zhang, J.M.; Zhao, H.Y.; Li, P.; Sun, H.Y. Understanding the photocatalytic mechanisms of the BiOI/Bi₂MoO₆ and BiOCl/Bi₂MoO₆ heterostructures: First-principles study. *J. Phys. Chem. Solids* **2020**, *146*, 109577. [[CrossRef](#)]
36. Wang, S.M.; Guan, Y.; Wang, L.P.; Zhao, W.; He, H.; Xiao, J.; Yang, S.G.; Sun, C. Fabrication of a novel bifunctional material of BiOI/Ag₃VO₄ with high adsorption–photocatalysis for efficient treatment of dye wastewater. *Appl. Catal. B Environ.* **2015**, *168–169*, 448–457. [[CrossRef](#)]
37. Ma, F.Q.; Yao, J.W.; Zhang, Y.F.; Wei, Y. Oxygen vacancy promoting adsorption property of BiOI microspheres modified with SDS. *Chin. Chem. Lett.* **2018**, *29*, 1689–1691. [[CrossRef](#)]
38. Ren, K.X.; Zhang, K.; Liu, J.; Luo, H.; Huang, Y.B.; Yu, X.B. Controllable synthesis of hollow/flower-like BiOI microspheres and highly efficient adsorption and photocatalytic activity. *CrystEngComm* **2012**, *14*, 4384–4390. [[CrossRef](#)]
39. Phuruangrat, A.; Ekthammathat, N.; Kuntalue, B.; Dumrongrojthanath, P.; Thongtem, S.; Thongtem, T. Hydrothermal synthesis, characterization, and optical properties of Ce doped Bi₂MoO₆ nanoplates. *J. Nanomater.* **2014**, *2014*, 934165.
40. Holzwarth, U.; Gibson, N. The Scherrer equation versus the “Debye-Scherrer equation”. *Nat. Nanotechnol.* **2011**, *6*, 534. [[CrossRef](#)]
41. Li, W.T.; Zheng, Y.F.; Yin, H.Y.; Song, X.C. Heterojunction BiOI/Bi₂MoO₆ nanocomposite with much enhanced photocatalytic activity. *J. Nanopart. Res.* **2015**, *17*, 271. [[CrossRef](#)]
42. Dumrongrojthanath, P.; Phuruangrat, A.; Thongtem, S.; Thongtem, T. Hydrothermal synthesis and characterization of visible light-driven I-doped Bi₂MoO₆ photocatalyst. *J. Iran. Chem. Soc.* **2018**, *16*, 733–739. [[CrossRef](#)]
43. Qin, L.; Li, Y.; Liang, F.; Li, L.; Lan, Y.; Li, Z.; Lu, X.; Yang, M.; Ma, D. A microporous 2D cobalt-based MOF with pyridyl sites and open metal sites for selective adsorption of CO₂. *Microporous Mesoporous Mater.* **2022**, *341*, 112098. [[CrossRef](#)]
44. Liu, Z.; Liu, X.Q.; Yu, C.L.; Wei, L.F.; Ji, H.B. Fabrication and characterization of I doped Bi₂MoO₆ microspheres with distinct performance for removing antibiotics and Cr(VI) under visible light illumination. *Sep. Purif. Technol.* **2020**, *247*, 116951. [[CrossRef](#)]
45. Sin, J.C.; Lam, S.M.; Zeng, H.; Lin, H.; Li, H.; Tham, K.O.; Mohamed, A.R.; Lim, J.W.; Qin, Z.Z. Magnetic NiFe₂O₄ nanoparticles decorated on N-doped BiOBr nanosheets for expeditious visible light photocatalytic phenol degradation and hexavalent chromium reduction via a Z-scheme heterojunction mechanism. *Appl. Surf. Sci.* **2021**, *559*, 559–562. [[CrossRef](#)]
46. Yang, Z.X.; Wang, R.Q.; Xu, L.J.; Liu, C.L.; Cheng, Y.; Jiang, Z.; Liu, Y.L.; Zhang, T.; Li, J.Y.; Liu, X.Z. Highly efficient flower-like Dy³⁺-doped Bi₂MoO₆ photocatalyst under simulated sunlight: Design, fabrication and characterization. *Opt. Mater.* **2021**, *116*, 111–114. [[CrossRef](#)]
47. Sun, X.M.; Lu, J.; Wu, J.; Guan, D.Y.; Liu, Q.Z.; Yan, N.Q. Enhancing photocatalytic activity on gas-phase heavy metal oxidation with self-assembled BiOI/BiOCl microflowers. *J. Colloid Interface Sci.* **2019**, *546*, 32–42. [[CrossRef](#)]
48. Xia, S.Q.; Jia, R.Y.; Feng, F.; Xie, K.; Li, H.X.; Jing, D.F.; Xu, X.T. Effect of solids retention time on antibiotics removal performance and microbial communities in an A/O-MBR process. *Bioresour. Technol.* **2012**, *106*, 36–43. [[CrossRef](#)]
49. Tang, W.H.; Zhang, Y.L.; Guo, H.G.; Liu, Y. Heterogeneous activation of peroxymonosulfate for bisphenol AF degradation with BiOI_{0.5}Cl_{0.5}. *RSC Adv.* **2019**, *9*, 14060–14071. [[CrossRef](#)]
50. Sun, G.T.; Shi, J.W.; Mao, S.M.; Ma, D.D.; He, C.; Wang, H.K.; Cheng, Y.H. Dodecylamine coordinated tri-arm CdS nanorod wrapped in intermittent ZnS shell for greatly improved photocatalytic H₂ evolution. *Chem. Eng. J.* **2022**, *429*, 132382. [[CrossRef](#)]
51. Zhang, L.; Liu, F.; Xiao, X.; Zuo, X.X.; Nan, J.M. Microwave synthesis of iodine-doped bismuth oxychloride microspheres for the visible light photocatalytic removal of toxic hydroxyl-contained intermediates of parabens: Catalyst synthesis, characterization, and mechanism insight. *Environ. Sci. Pollut. Res. Int.* **2019**, *26*, 28871–28883. [[CrossRef](#)] [[PubMed](#)]
52. Feng, J.W.; Huang, H.W.; Yu, S.X.; Dong, F.; Zhang, Y.H. A self-sacrifice template route to iodine modified BiOIO₃: Band gap engineering and highly boosted visible-light active photoreactivity. *Phys. Chem. Chem. Phys.* **2016**, *18*, 7851–7859. [[CrossRef](#)]
53. Zhang, K.; Zhang, D.Q.; Liu, J.; Ren, K.X.; Luo, H.; Peng, Y.J.; Li, G.S.; Yu, X.B. A novel nanoreactor framework of iodine-incorporated BiOCl core-shell structure: Enhanced light-harvesting system for photocatalysis. *CrystEngComm* **2012**, *14*, 700–707. [[CrossRef](#)]
54. Singh, S.; Sahoo, R.K.; Shinde, N.M.; Yun, J.M.; Mane, R.S.; Chung, W.; Kim, K.H. Asymmetric faradaic assembly of Bi₂O₃ and MnO₂ for a high-performance hybrid electrochemical energy storage device. *RSC Adv.* **2019**, *9*, 32154–32164. [[CrossRef](#)] [[PubMed](#)]
55. Li, H.P.; Liu, J.Y.; Hou, W.G.; Du, N.; Zhang, R.J.; Tao, X.T. Synthesis and characterization of g-C₃N₄/Bi₂MoO₆ heterojunctions with enhanced visible light photocatalytic activity. *Appl. Catal. B Environ.* **2014**, *160–161*, 89–97. [[CrossRef](#)]
56. Xu, Y.S.; Zhang, W.D. Monodispersed Ag₃PO₄ nanocrystals loaded on the surface of spherical Bi₂MoO₆ with enhanced photocatalytic performance. *Dalton Trans.* **2013**, *42*, 1094–1101. [[CrossRef](#)]

57. Hou, J.H.; Jiang, K.; Shen, M.; Wei, R.; Wu, X.G.; Idrees, F.; Cao, C.B. Micro and nano hierarchical structures of BiOI/activated carbon for efficient visible-light-photocatalytic reactions. *Sci. Rep.* **2017**, *7*, 11665. [[CrossRef](#)]
58. Tang, Y.F.; Lin, T.P.; Jiang, C.J.; Zhao, Y.M.; Ai, S.J. Renewable adsorbents from carboxylate-modified agro-forestry residues for efficient removal of methylene blue dye. *J. Phys. Chem. Solids* **2021**, *149*, 149–151. [[CrossRef](#)]
59. Wang, Y.T.; He, L.Y.; Dang, G.Y.; Li, H.; Li, X.L. Polypyrrole-functionalized magnetic Bi₂MoO₆ nanocomposites as a fast, efficient and reusable adsorbent for removal of ketoprofen and indomethacin from aqueous solution. *J. Colloid Interface Sci.* **2021**, *592*, 51–65. [[CrossRef](#)]
60. Guo, Y.P.; Zhao, J.Z.; Zhang, H.; Yang, S.F.; Qi, J.R.; Wang, Z.C.; Xu, H.D. Use of rice husk-based porous carbon for adsorption of Rhodamine B from aqueous solutions. *Dyes Pigment.* **2005**, *66*, 123–128. [[CrossRef](#)]
61. Oyedade, O.A.; Nyamori, V.O.; Martincigh, B.S.; Jonnalagadda, S.B. Effectiveness of carbon nanotube–cobalt ferrite nanocomposites for the adsorption of rhodamine B from aqueous solutions. *RSC Adv.* **2015**, *5*, 22724–22739. [[CrossRef](#)]
62. Jiang, L.; Wen, Y.Y.; Zhu, Z.J.; Liu, X.F.; Shao, W. A Double cross-linked strategy to construct graphene aerogels with highly efficient methylene blue adsorption performance. *Chemosphere* **2021**, *265*, 129169. [[CrossRef](#)] [[PubMed](#)]
63. Xiao, J.X.; Chen, Y.; Xue, M.; Ding, R.; Kang, Y.; Tremblay, P.L.; Zhang, T. Fast-growing cyanobacteria bio-embedded into bacterial cellulose for toxic metal bioremediation. *Carbohydr. Polym.* **2022**, *295*, 119881. [[CrossRef](#)] [[PubMed](#)]
64. Xiao, X.; Wang, Y.H.; Cui, B.W.; Zhang, X.B.; Zhang, D.G.; Xu, X.Y. Preparation of MoS₂ nanoflowers with rich active sites as an efficient adsorbent for aqueous organic dyes. *New J. Chem.* **2020**, *44*, 4558–4567. [[CrossRef](#)]
65. Tang, S.; Xia, D.S.; Yao, Y.; Chen, T.Y.; Sun, J.; Yin, Y.J.; Shen, W.; Peng, Y.X. Dye adsorption by self-recoverable, adjustable amphiphilic graphene aerogel. *J. Colloid Interface Sci.* **2019**, *554*, 682–691. [[CrossRef](#)]
66. Godiya, C.B.; Kumar, S.; Xiao, Y.H. Amine functionalized egg albumin hydrogel with enhanced adsorption potential for diclofenac sodium in water. *J. Hazard. Mater.* **2020**, *393*, 122417. [[CrossRef](#)] [[PubMed](#)]
67. Zamani, S.; Tabrizi, N.S. Removal of methylene blue from water by graphene oxide aerogel: Thermodynamic, kinetic, and equilibrium modeling. *Res. Chem. Intermed.* **2014**, *41*, 7945–7963. [[CrossRef](#)]
68. Kinniburgh, D.G. General purpose adsorption isotherms. *Environ. Sci. Technol.* **1986**, *20*, 895–904. [[CrossRef](#)]
69. Wu, Z.B.; Zhong, H.; Yuan, X.Z.; Wang, H.; Wang, L.L.; Chen, X.H.; Zeng, G.M.; Wu, Y. Adsorptive removal of methylene blue by rhamnolipid-functionalized graphene oxide from wastewater. *Water Res.* **2014**, *67*, 330–344. [[CrossRef](#)]
70. Ding, L.L.; Zou, B.; Gao, W.; Liu, Q.; Wang, Z.C.; Guo, Y.P.; Wang, X.F.; Liu, Y.H. Adsorption of Rhodamine-B from aqueous solution using treated rice husk-based activated carbon. *Colloid Surf. A* **2014**, *446*, 1–7. [[CrossRef](#)]
71. Lian, L.L.; Guo, L.P.; Guo, C.J. Adsorption of Congo red from aqueous solutions onto Ca-bentonite. *J. Hazard. Mater.* **2009**, *161*, 126–131. [[CrossRef](#)]
72. Zhao, G.X.; Li, J.X.; Ren, X.M.; Chen, C.L.; Wang, X.K. Few-layered graphene oxide nanosheets as superior sorbents for heavy metal ion pollution management. *Environ. Sci. Technol.* **2011**, *45*, 10454–10462. [[CrossRef](#)] [[PubMed](#)]
73. Costa, L.N.; Nobre, F.X.; Lobo, A.O.; De Matos, J.M.E. Photodegradation of ciprofloxacin using Z-scheme TiO₂/SnO₂ nanostructures as photocatalyst. *Environ. Nanotechnol. Monit. Manag.* **2021**, *16*, 100466.
74. Zhao, M.; Liu, P. Adsorption of methylene blue from aqueous solutions by modified expanded graphite powder. *Desalination* **2009**, *249*, 331–336. [[CrossRef](#)]
75. Kaewmanee, T.; Wannapop, S.; Phuruangrat, A.; Thongtem, T.; Thongtem, S. Solvothermal synthesis of BiOBr_xI_{1-x} (x = 0.0–1.0) solid solutions used for adsorption and photodegradation of cationic and anionic dyes. *Inorg. Chem. Commun.* **2021**, *134*, 109054. [[CrossRef](#)]

Disclaimer/Publisher’s Note: The statements, opinions and data contained in all publications are solely those of the individual author(s) and contributor(s) and not of MDPI and/or the editor(s). MDPI and/or the editor(s) disclaim responsibility for any injury to people or property resulting from any ideas, methods, instructions or products referred to in the content.